

# Image-domain waveform inversion with the adjoint-state method

Tongning Yang and Paul Sava

*Center for Wave Phenomena, Colorado School of Mines*

## ABSTRACT

Waveform inversion is a velocity model building technique based on full seismograms as the input and seismic wavefields as the information carrier. Conventional waveform inversion is implemented in the data-domain. Similar techniques can be formulated in the image domain, with seismic image as the input and seismic wavefields as the information carrier. The objective function for image-domain waveform inversion is designed to optimize the coherency of reflections in extended common-image gathers. The function applies a penalty operator to the gathers, thus highlighting inaccuracies due to the velocity model error. Minimizing the objective function optimizes the model and improves the image quality. The gradient of the objective function is computed using the adjoint-state method in a similar way to the data-domain implementation. We present a parallel derivation for waveform inversion in data-domain and image-domain, and show that these two approaches are only different in the choice of the objective function. The image-domain formulation is implemented with various types of extended image gathers with almost identical workflows. The results obtained from these approaches applied to the same synthetic model are quite different. The methods implemented with space-lag gathers and common-image-point gathers recover the model and improve the image quality. The approach with time-lag gathers is less effective to reconstruct the model compared to other formulations because it is less sensitive in capturing the image incoherency due to the model error.

**Key words:** waveform inversion, velocity analysis, extended images, adjoint state method

## 1 INTRODUCTION

In regions characterized by complex subsurface structure, prestack wave-equation depth migration, (i.e. one-way wave-equation migration or reverse-time migration), is a powerful tool for accurately imaging the earth's interior (Gray et al., 2001; Etgen et al., 2009). However, the quality of the final image greatly depends on the accuracy of the velocity model. Thus, a key challenge for seismic imaging in complex geology is an accurate determination of the velocity model in the area under investigation (Symes, 2008; Woodward et al., 2008; Virieux and Operto, 2009).

Waveform inversion (WI) represents a family of techniques for velocity model building using seismic wavefields (Tarantola, 1984; Woodward, 1992; Pratt, 1999; Sirgue and Pratt, 2004; Plessix, 2006; Vigh and Starr, 2008; Plessix, 2009; Symes, 2009). This type of methodology, although usually regarded as one of the costliest techniques for velocity estima-

tion, has been gaining momentum in recent years, mainly due to its accuracy and to advances in computing technology. A key component of WI is wavefield simulation using a wave-equation, typically an acoustic wave-equation. Usually, WI is implemented in the data-domain, by adjusting the velocity model such that simulated and recorded data match (Tarantola, 1984; Pratt, 1999). This match is based on the strong assumption that the wave-equation used for simulation is consistent with the earth, which is unlikely to be the case when the earth is characterized by strong (poro)elastic effects. Significant effort is often directed toward removing the components of the recorded data that are inconsistent with the assumptions used.

Another key component of WI is the objective function (OF) used to measure the match between the simulated and recorded data. It is assumed that the OF is more-or-less convex, which allows for its minimization using gradient-based techniques. Thus, successful implementation of WI requires

an effective (i.e. quick and robust) implementation of the gradient of the objective function.

An effective gradient calculation is based on the adjoint state method (Plessix, 2006; Symes, 2009). In summary, this method consists of the following steps: (1) compute the *state variables*, i.e. the seismic wavefields obtained from the source by forward modeling; (2) compute the *adjoint source*, i.e. a calculation based on the OF and on the state variables; (3) compute the *adjoint state variables*, i.e. the seismic wavefields obtained from the adjoint source by backward modeling; (4) compute the *gradient* using the state and adjoint state variables.

Velocity model building methods using seismic wavefields can also be implemented in the image domain instead of the data domain. Instead of minimizing the data misfit, the techniques in this category update the velocity model by optimizing the image, which is the cross-correlation of wavefields extrapolated from the data and from the known source function. Such techniques are motivated by the fact that the quality of the image is optimized when the data are migrated with the correct velocity model, as stated by the semblance principle (Al-Yahya, 1989; Yilmaz, 2001). Since images are obtained using full seismograms, and velocity estimation also uses seismic wavefields as the information carrier, one can consider such techniques as a particular type of WI, and we refer to them as image-domain WI.

Sava and Biondi (2004a,b) introduce the concept of wave-equation migration velocity analysis (WEMVA). The core of the method is to linearize the downward continuation operator and to establish a linear relationship between the model perturbation and image perturbation. Sava et al. (2005) demonstrate the application of WEMVA to velocity model building in complex regions, and Sava and Vlad (2008) illustrate the detailed numerical implementation of WEMVA. Because the technique uses wavefields in the optimization procedure, WEMVA is capable of handling complicated wave-propagation phenomena such as multi-pathing. In addition, the band-limited character of the method better approximates wave propagation in the subsurface. Essentially, the idea behind the technique is to optimize the coherency of reflection events in common-image gathers (CIGs) via velocity model updating.

Among the various types of CIGs, space-lag CIGs (subsurface-offset) (Rickett and Sava, 2002; Shen and Calandra, 2005) and angle-domain CIGs (Sava and Fomel, 2003; Biondi and Symes, 2004) are two popular choices used in the Differential semblance optimization (DSO). Symes and Carazzone (1991) propose the criterion of measuring coherency for offset CIGs and establish the theory for DSO. The concept is then generalized to space-lag CIGs (Shen and Calandra, 2005; Shen and Symes, 2008) because space-lag CIGs obtained with wave-equation migration are free of artifacts usually found in conventional offset gathers, and thus they are suitable for applications in complex earth models. Shen and Symes (2008) also compare the implementation of DSO with angle-domain CIGs and space-lag CIGs and conclude that the inversion with angle-domain CIGs is worse because the angle-

domain penalty operator has a larger condition number and slows down the convergence of the inversion.

Another choice of gathers for WEMVA are time-lag CIGs (Sava and Fomel, 2006). Yang and Sava (2010c) propose an WEMVA approach using time-lag CIGs. The method applies focusing analysis (Nemeth, 1995; Wang et al., 2005) to measure the coherency of the gathers and optimizes the model by penalizing the non-focused reflections at non-zero time-lag due to the velocity error. As pointed out by Sava and Fomel (2006) and Yang and Sava (2010a), the resolution of time-lag CIGs is lower than that of space-lag CIGs. However, because of the relatively cheap computational cost and storage requirement, time-lag CIGs are more popular for imaging 3-D wide-azimuth surveys. Furthermore, time-lag CIGs can be a good alternative for velocity model building when moveout information is difficult to extract from space-lag or angle gathers.

Sava and Vasconcelos (2011) and Vasconcelos et al. (2010) propose extended common-image-point gathers (CIPs) as an alternative to conventional space- or time-lag CIGs. Extended CIPs are constructed sparsely on reflection events with both time-lags and space-lags. Such a construction brings two major advantages. First, the construction of a complete lag vector avoids the bias toward nearly-horizontal reflections, and thus the gathers are free of the artifacts generated by steeply dipping reflections in conventional CIGs. Second, the sparse sampling of the gathers provide an efficient and flexible way to extract the information about the accuracy of the velocity model from the subsurface. Yang and Sava (2010b) demonstrate the construction of WEMVA operators with CIPs and Sava and Vlad (2011) propose a new angle-decomposition method using CIPs for wide-azimuth surveys.

In this paper, we compare the workflows for data-domain and image-domain WI. We focus on image-domain formulation and demonstrate the implementations with time-lag CIGs, space-lag CIGs, and extended CIPs. We analyze the similarity and differences of image-domain WI using all types of extended images and illustrate the techniques using 2D synthetic examples.

## 2 THEORY

In this section, we start with the formulation of a data-domain implementation of WI using a correlation-type objective function (OF). The gradient of the OF is computed by applying the adjoint state-method (Plessix, 2006; Symes, 2009). Such a workflow is the common formulation of WI in the data-domain (Virieux and Operto, 2009). Next, we show how this formulation can be generalized to image-domain WI, with different input image gathers, e.g. time-lag CIGs, space-lag CIGs, and extended CIPs.

### 2.1 Data-domain WI

#### 2.1.1 State variables

The state variables relate the objective function to the model parameters. We define the seismic wavefields as the state vari-

ables for data-domain WI, and these wavefields are obtained by solving the acoustic wave-equation

$$\mathcal{L}(\mathbf{x}, \omega, m) u_s(\mathbf{e}, \mathbf{x}, \omega) = f_s(\mathbf{e}, \mathbf{x}, \omega), \quad (1)$$

where  $\mathcal{L}$  denotes the wave operator,  $u_s$  is the simulated wavefield,  $f_s$  is the source data which can be described by a point source, or a plane source, etc,  $m$  are the model parameters,  $\mathbf{e}$  is the experiment index,  $\omega$  is the frequency, and  $\mathbf{x}$  are the space coordinates  $\{x, y, z\}$ .

### 2.1.2 Adjoint source

The adjoint sources are used to model the adjoint state variables, and these sources are computed based on the particular choice of the OF and state variables. Conventional WI is an inverse problem with the model found by minimizing an OF defined using the difference between the observed and simulated wavefields,  $u_o$  and  $u_s$  (Tarantola, 1984; Pratt, 1999):

$$\mathcal{H}_D = \sum_{\mathbf{e}} \frac{1}{2} \|K_D(\mathbf{e}, \mathbf{x}) (u_s(\mathbf{e}, \mathbf{x}, \omega) - u_o(\mathbf{e}, \mathbf{x}, \omega))\|_{\mathbf{x}, \omega}^2. \quad (2)$$

Here,  $K_D$  is a mask operator which limits the definition of the OF to specific locations, e.g. to positions on the surface. Such a common OF suffers, among other things, from cycle skipping due to the oscillatory nature of the subtracted wavefields.

An alternative OF uses the correlation of the observed and simulated wavefields, instead of their difference (van Leeuwen and Mulder, 2010):

$$\mathcal{H}_C = \sum_{\mathbf{e}} \frac{1}{2} \|K_D(\mathbf{e}, \mathbf{x}) P(\tau) c(\mathbf{e}, \mathbf{x}, \tau)\|_{\mathbf{x}, \tau}^2. \quad (3)$$

Here,  $c$  is the correlation between the observed and simulated wavefields:

$$c(\mathbf{e}, \mathbf{x}, \tau) = \sum_{\omega} u_s(\mathbf{e}, \mathbf{x}, \omega) \overline{u_o(\mathbf{e}, \mathbf{x}, \omega)} e^{2i\omega\tau}, \quad (4)$$

where the overline indicates complex conjugation, and  $P(\tau)$  is an operator penalizing correlation energy outside zero time-lag:

$$P(\tau) = |\tau|, \quad (5)$$

where  $\tau$  is the cross-correlation time-lag.

The adjoint sources are computed as the derivative of the OF ( $\mathcal{H}_C$ ) with respect to the state variables  $u_s$ :

$$g_s(\mathbf{e}, \mathbf{x}, \omega) = K_D(\mathbf{e}, \mathbf{x}) \overline{K_D(\mathbf{e}, \mathbf{x})} \times \sum_{\tau} P(\tau) \overline{P(\tau)} \Re \left( c(\mathbf{e}, \mathbf{x}, \tau) u_o(\mathbf{e}, \mathbf{x}, \omega) e^{-2i\omega\tau} \right), \quad (6)$$

where  $\Re$  indicates that we take the real part of the complex wavefields. Equation 6 demonstrate the dependence of the adjoint source on the OF and state variables.

### 2.1.3 Adjoint state variables

The adjoint state variable  $a_s$  is the wavefield obtained by backward modeling using the adjoint source  $g_s$ :

$$\mathcal{L}^*(\mathbf{x}, \omega, m) a_s(\mathbf{e}, \mathbf{x}, \omega) = g_s(\mathbf{e}, \mathbf{x}, \omega), \quad (7)$$

where the \* sign indicates that the receiver wavefield is constructed by modeling backward in time, i.e. by using the adjoint operator  $\mathcal{L}^*$ .

### 2.1.4 Gradient

The gradient of the OF is calculated via the expression

$$\frac{\partial \mathcal{H}_C}{\partial m} = \sum_{\mathbf{e}} \sum_{\omega} \frac{\partial \mathcal{L}}{\partial m} \left( u_s(\mathbf{e}, \mathbf{x}, \omega) \overline{a_s(\mathbf{e}, \mathbf{x}, \omega)} \right). \quad (8)$$

If we define  $\mathcal{L}$  as a Helmholtz wave operator  $-\omega^2 m - \Delta$  where  $m$  is slowness square, then  $\frac{\partial \mathcal{L}}{\partial m}$  is simply  $-\omega^2$ .

## 2.2 Image-domain WI with time-lag CIGs

A similar procedure can be implemented in the image-domain with extended images obtained by wave-equation migration (downward continuation or reverse-time). We first illustrate the implementation with time-lag common-image gathers (CIGs) (Sava and Fomel, 2006).

### 2.2.1 State variables

The state variables are represented by the source and receiver wavefields simulated from the source wavelet and the recorded data:

$$\begin{bmatrix} \mathcal{L}(\mathbf{x}, \omega, m) & 0 \\ 0 & \mathcal{L}^*(\mathbf{x}, \omega, m) \end{bmatrix} \begin{bmatrix} u_s(\mathbf{e}, \mathbf{x}, \omega) \\ u_r(\mathbf{e}, \mathbf{x}, \omega) \end{bmatrix} = \begin{bmatrix} f_s(\mathbf{e}, \mathbf{x}, \omega) \\ f_r(\mathbf{e}, \mathbf{x}, \omega) \end{bmatrix}. \quad (9)$$

Here,  $\mathcal{L}$  and  $\mathcal{L}^*$  are the same forward and backward wave propagation operators as in the data-domain WI formulation,  $u_s$  and  $u_r$  are the simulated source and receiver wavefields,  $f_s$  and  $f_r$  are the source and record data, other notations are identical to the preceding case. In contrast to the data-domain implementation where we only extrapolate the source function forward in time, for image-domain WI we extrapolate both the source function and the data forward and backward in time, respectively.

### 2.2.2 Adjoint source

An image-domain OF is formulated to minimize image inconsistencies caused by the model errors. Thus, the optimization process simultaneously improves the model and the image quality. The OF based on time-lag CIGs is constructed as

$$\mathcal{H}_\tau = \frac{1}{2} \|K_I(\mathbf{x}) P(\tau) r(\mathbf{x}, \tau)\|_{\mathbf{x}, \tau}^2, \quad (10)$$

where  $r(\mathbf{x}, \tau)$  is the time-lag extended image (Sava and Fomel, 2006) obtained by correlation of the source and receiver wavefields, followed by summation over experiments:

$$r(\mathbf{x}, \tau) = \sum_{\mathbf{e}} \sum_{\omega} \overline{u_s(\mathbf{e}, \mathbf{x}, \omega)} u_r(\mathbf{e}, \mathbf{x}, \omega) e^{2i\omega\tau}, \quad (11)$$

and an example of the penalty operator  $P(\tau)$  is

$$P(\tau) = |\tau|. \quad (12)$$

As for the preceding case, this penalty operator is not unique. The adjoint sources are computed as the derivatives of the OF  $\mathcal{H}_\tau$  in equation 10 with respect to the state variables  $u_s$  and  $u_r$ , respectively:

$$\begin{aligned} g_s(\mathbf{e}, \mathbf{x}, \omega) &= K_I(\mathbf{x}) \overline{K_I(\mathbf{x})} \times \\ &\sum_{\tau} P(\tau) \overline{P(\tau)} r(\mathbf{x}, \tau) u_r(\mathbf{e}, \mathbf{x}, \omega) e^{-2i\omega\tau}, \\ g_r(\mathbf{e}, \mathbf{x}, \omega) &= K_I(\mathbf{x}) \overline{K_I(\mathbf{x})} \times \\ &\sum_{\tau} P(\tau) \overline{P(\tau)} r(\mathbf{x}, \tau) u_s(\mathbf{e}, \mathbf{x}, \omega) e^{-2i\omega\tau}. \end{aligned} \quad (13)$$

### 2.2.3 Adjoint state variables

The adjoint state variable  $a_s$  and  $a_r$  are the wavefields obtained by backward and forward modeling using the corresponding adjoint sources:

$$\begin{bmatrix} \mathcal{L}^*(\mathbf{x}, \omega, m) & 0 \\ 0 & \mathcal{L}(\mathbf{x}, \omega, m) \end{bmatrix} \begin{bmatrix} a_s(\mathbf{e}, \mathbf{x}, \omega) \\ a_r(\mathbf{e}, \mathbf{x}, \omega) \end{bmatrix} = \begin{bmatrix} g_s(\mathbf{e}, \mathbf{x}, \omega) \\ g_r(\mathbf{e}, \mathbf{x}, \omega) \end{bmatrix}. \quad (14)$$

### 2.2.4 Gradient

The computation of the gradient is simply

$$\begin{aligned} \frac{\partial \mathcal{H}_\tau}{\partial m} &= \sum_{\mathbf{e}} \sum_{\omega} \frac{\partial \mathcal{L}}{\partial m} \times \\ &\left( u_s(\mathbf{e}, \mathbf{x}, \omega) \overline{a_s(\mathbf{e}, \mathbf{x}, \omega)} + u_r(\mathbf{e}, \mathbf{x}, \omega) \overline{a_r(\mathbf{e}, \mathbf{x}, \omega)} \right). \end{aligned} \quad (15)$$

The gradient consists of the correlations of the state variables and adjoint state variables on the source and receiver sides.

## 2.3 Image-domain WI with space-lag CIGs

An alternative image-domain WI can be implemented using space-lag CIGs (Rickett and Sava, 2002; Shen and Calandra, 2005).

### 2.3.1 State variables

Space-lag extended images are obtained by cross-correlating the wavefields. Thus, the state variables are also represented by source and receiver wavefields  $u_s$  and  $u_r$  constructed similarly using equations 9.

### 2.3.2 Adjoint source

The OF for space-lag CIGs is defined as

$$\mathcal{H}_\lambda = \frac{1}{2} \|K_I(\mathbf{x}) P(\lambda) r(\mathbf{x}, \lambda)\|_{\mathbf{x}, \lambda}^2, \quad (16)$$

where  $r(\mathbf{x}, \lambda)$  are space-lag extended images obtained by correlation of space-shifted source and receiver wavefields, followed by summation over experiments:

$$\begin{aligned} r(\mathbf{x}, \lambda) &= \sum_{\mathbf{e}} \sum_{\omega} \overline{u_s(\mathbf{e}, \mathbf{x} - \lambda, \omega)} u_r(\mathbf{e}, \mathbf{x} + \lambda, \omega) \\ &= \sum_{\mathbf{e}} \sum_{\omega} T(-\lambda) \overline{u_s(\mathbf{e}, \mathbf{x}, \omega)} T(\lambda) u_r(\mathbf{e}, \mathbf{x}, \omega). \end{aligned} \quad (17)$$

The operator  $T$  represents the space shift applied to the wavefields and is defined as

$$T(\lambda) u(\mathbf{e}, \mathbf{x}, \omega) = u(\mathbf{e}, \mathbf{x} + \lambda, \omega). \quad (18)$$

A common practice is to restrict the space-lags in the horizontal directions only, i.e.  $\lambda = \{\lambda_x, \lambda_y, 0\}$ . The penalty operator  $P(\lambda)$  is

$$P(\lambda) = |\lambda|. \quad (19)$$

The operator  $P_\lambda$  is a first-order differential operator which annihilates reflections focused at zero lag and highlights the residual moveout at non-zero lags. Therefore, the OF is minimized when the reflections focus at zero lag, an indication of the correct velocity model. The adjoint sources are computed as the derivatives of the OF  $\mathcal{H}_\lambda$  in equation 16 with respect to the state variables  $u_s$  and  $u_r$ , respectively:

$$\begin{aligned} g_s(\mathbf{e}, \mathbf{x}, \omega) &= K_I(\mathbf{x}) \overline{K_I(\mathbf{x})} \times \\ &\sum_{\lambda} T(-\lambda) P(\lambda) \overline{P(\lambda)} r(\mathbf{x}, \lambda) T(\lambda) u_r(\mathbf{e}, \mathbf{x}, \omega), \\ g_r(\mathbf{e}, \mathbf{x}, \omega) &= K_I(\mathbf{x}) \overline{K_I(\mathbf{x})} \times \\ &\sum_{\lambda} T(\lambda) P(\lambda) \overline{P(\lambda)} r(\mathbf{x}, \lambda) T(-\lambda) u_s(\mathbf{e}, \mathbf{x}, \omega). \end{aligned} \quad (20)$$

### 2.3.3 Adjoint state variables

The adjoint state variable  $a_s$  and  $a_r$  are computed using equation 14 given the adjoint sources defined in equation 20.

### 2.3.4 Gradient

The computation of the gradient is the same as in equation 15.

## 2.4 Image-domain WI with extended CIPs

### 2.4.1 State variables

Extended CIPs are obtained by applying non-zero space- and time-lag cross-correlation imaging condition to the wavefields at selected points in the image. Again, the state variables are the source and receiver wavefields  $u_s$  and  $u_r$  simulated with equations 9.

### 2.4.2 Adjoint source

Sava and Vasconcelos (2011) analyze the kinematic characteristics of reflections in extended CIPs and point out that reflections focus at zero space- and time-lags when the migration velocity is correct. Therefore, the OF for extended CIPs is defined as

$$\mathcal{H}_{\lambda, \tau} = \frac{1}{2} \|K_I(\mathbf{x}) P(\lambda, \tau) r(\mathbf{x}, \lambda, \tau)\|_{\mathbf{x}, \lambda, \tau}^2, \quad (21)$$

where

$$\begin{aligned} r(\mathbf{x}, \lambda, \tau) &= \sum_{\mathbf{e}} \sum_{\omega} \overline{u_s(\mathbf{e}, \mathbf{x} - \lambda, \omega)} u_r(\mathbf{e}, \mathbf{x} + \lambda, \omega) e^{2i\omega\tau} \\ &= \sum_{\mathbf{e}} \sum_{\omega} T(-\lambda) \overline{u_s(\mathbf{e}, \mathbf{x}, \omega)} T(\lambda) u_r(\mathbf{e}, \mathbf{x}, \omega) e^{2i\omega\tau}. \end{aligned} \quad (22)$$

The masking operator  $K_I(\mathbf{x})$  here is different from those in preceding situations, it restricts the construction of extended images on individual locations only. In other words, the CIPs are constructed on reflectors only, and sampled sparsely in the image. As a result, CIPs provide an effective and efficient way to extract velocity information from migrated images for two reasons. First, no gathers are computed in areas without reflections so that the computational cost is reduced. Second, CIPs can be computed on very steep reflectors where conventional CIGs fail to access the information contained in these reflections. An example of a penalty operator  $P(\lambda, \tau)$  for vector lags is

$$P(\lambda, \tau) = \sqrt{|\lambda \cdot \mathbf{q}|^2 + (V\tau)^2}. \quad (23)$$

Here  $\mathbf{q}$  is the unit vector in the reflection plane and  $V$  represents the local migration velocity. If we only consider the case of horizontal space-lags, the penalty operator can be simplified as

$$P(\lambda, \tau) = \sqrt{|\lambda|^2 + (V\tau)^2}. \quad (24)$$

The operator  $P(\lambda, \tau)$  is defined to penalize the energy outside zero space- and time-lags, which indicates the existence of the velocity model error. Reflections in CIPs focus at zero lag when the correct velocity model is used for migration, or residual moveout at non-zero lags when the model is incorrect. Therefore, the defocused energy outside zero space lag is enhanced by the operator  $P(\lambda, \tau)$  and forms the basis for optimization. The adjoint sources, although more complicated because more lags are involved, are also computed as the derivatives of the OF  $\mathcal{H}_{\lambda, \tau}$  in equation 21 with respect to the state variables  $u_s$  and  $u_r$ , respectively:

$$\begin{aligned} g_s(\mathbf{e}, \mathbf{x}, \omega) &= K_I(\mathbf{x}) \overline{K_I(\mathbf{x})} \times \\ &\sum_{\lambda, \tau} T(-\lambda) P(\lambda, \tau) \overline{P(\lambda, \tau)} r(\lambda, \tau) T(\lambda) u_r(\mathbf{e}, \mathbf{x}, \omega) e^{-2i\omega\tau}, \\ g_r(\mathbf{e}, \mathbf{x}, \omega) &= K_I(\mathbf{x}) \overline{K_I(\mathbf{x})} \times \\ &\sum_{\lambda, \tau} T(\lambda) P(\lambda, \tau) \overline{P(\lambda, \tau)} r(\lambda, \tau) T(-\lambda) u_s(\mathbf{e}, \mathbf{x}, \omega) e^{-2i\omega\tau}. \end{aligned} \quad (25)$$

### 2.4.3 Adjoint state variables

The adjoint state variable  $a_s$  and  $a_r$  are computed using equation 14 given the sources defined in equation 25.

### 2.4.4 Gradient

The gradient corresponding to OF in equation 21 is the same as in equation 15.

## 2.5 Summary

Given the objective function and the gradient, the inverse problem can be solved using a gradient-based iterative algorithm such as the nonlinear conjugate-gradient method (Parker, 1994). It is apparent that choices made in defining the state variables and the OF determine the character of the adjoint state variables. The formulation of OF defines the adjoint sources used to model adjoint state variables. Such dependencies highlight the relation of the OF and the state variables to the computation of the gradient.

We conclude that WI can be implemented in either data-domain or image-domain using a similar formulation. The major differences between these approaches consist of the definition of the OF and the computation of the gradient, especially when multiple seismic experiments (e.g. shots) are involved. In all cases we use the same wave-equation with the same data as boundary and initial conditions. Thus, all these methods are just alternative implementations of waveform inversion.

More commonality can be found when we examine the image-domain WI formulations. The definition of the state variables is the same. The computation of the adjoint state variables is identical for the various types of extended images. The difference comes merely from the choice of image gathers and the corresponding construction of OF. Such differences result in distinct adjoint sources for each problem, and therefore, different gradients.

Finally, we emphasize that for all types of WI, there are many possibilities for the penalty operators and thus the OFs are not unique. These choices give us the freedom to formulate the problem in a flexible way based on the specific configuration of the application.

## 3 EXAMPLES

We test the methods discussed in the preceding section with a model consisting of a smooth background with two Gaussian variations of opposite sign and five embedded horizontal reflectors. The true model is shown in Figure 1(a), and the magnitude of the variations are negative 15% of the background (left) and positive 15% of the background (right). The initial model is the smooth background, as shown in Figure ?? . Figure 1(b) and 1(c) display the images migrated with the true and initial models, respectively. As the low velocity variation generates wavefield triplication and multi-pathing, the incorrect velocity model distorts the reflectors below the variation in the

image. The target of the inversion is to recover these two variations. Here we apply image-domain WI with time-lag CIGs, space-lag CIGs, and extended CIPs to solve the same problem and evaluate the difference of the results. The inverse problems are solved by the nonlinear conjugate gradient method (Parker, 1994), and we stop after 15 iterations.

First, we examine image-domain WI implemented with time-lag CIGs. An example of the gathers migrated with the initial model and the penalty operator are shown in Figure 2(a) and 2(b). Figure 12(a) shows the OF evaluated as a function of iterations. Notice that the OF only decreases 10% after 15 iterations. This observation implies that this OF is less sensitive to the velocity model error. The reason might be attributed to the fact that reflections in time-lag CIGs spread the energy to non-zero lags even when the velocity is correct, as indicated by the events in Figure 2(a). As a result, the OF does not vary too much as a function of the model change. The inverted model and the corresponding migrated image are shown in Figure 3(b) and 3(c). Although the image migrated with the inverted model is improved, as the reflectors are more coherent, we cannot distinguish the Gaussian variations from the inverted model.

Next, we test the formulated using space-lag CIGs on the same model. Figure 5(a) and 5(b) plot an example of space-lag CIGs and the corresponding penalty operator proposed by Shen and Symes (2008). The CIGs are constructed with the initial model, thus we can observe the defocused reflections at non-zero space-lags. The inversion converges in about 10 iterations, as shown in Figure 12(b). The inverted model is depicted in Figure 6(b), and we can distinguish the Gaussian variations in the inverted model. This observation indicates the success of the inversion. The distortions of the image are eliminated, as seen in Figure 6(c). Also, the comparison of the CIGs shown in Figure 7(a) - 7(b) further confirms the improvements for the image quality, as the reflections in the gathers after the inversion are more focused at zero lag and most of the residual moveout at non-zero space-lags is eliminated.

Finally, we address the same problem with extended CIPs. Figure 8 show the same image as in Figure 1(c) overlain with the locations of the CIPs. The locations are selected by an automatic image-guided method (Cullison, 2011). Notice that the CIPs are only sampled on the reflectors influenced by the velocity error. Figure 9(a) shows an example of CIPs constructed at  $x = 1.5$  km,  $z = 1.53$  km. Here, we can observe additional events around  $-0.2$ s and  $0.2$ s in Figure 9(a). These events are images of the reflectors above and below which are introduced by the time-shift of the extended imaging condition. Since the penalty operator and the OF are defined based on the assumption that there is only one event in the gather, we consider these additional reflections as crosstalk and remove them by incorporating a mute window into the penalty operator, as shown in Figure 9(b). Figure 12(c) depicts the OF as a function of the iterations. Although subtle oscillation occurs at later iterations, the overall trend of the OF still decreases. This indicates the convergence of the inversion. The inverted model is shown in Figure 10(b). The reconstruction of the variations help improving the quality of the migrated image, as shown in

Figure 10(c). The distortion of the reflectors is corrected, and the images below the anomalies become more continuous and coherent. The improvement of the image quality can be further verified by comparing the CIPs before and after the inversion, since the reflections crossing the origin of the gathers are more focused, as seen in Figure 11(c) and 11(d).

### 3.1 Summary

To compare the results from different methods, we first examine their OFs of depicted in Figure 12(a) - 12(c). As shown in the plots, the inversions with space-lag CIGs and CIPs are converged in about 10 iterations, and the corresponding OFs decrease to 50% of the initial values. In contrast, the inversion with time-lag CIGs can hardly be considered as converged because the OF only decreases about 10% of the initial value. Next, we compare the difference between true anomaly and inverted anomaly from all methods. In Figure 13(b) and 13(c), we observe that the space-lag CIGs and CIPs inversion reconstruct the position and magnitude of the anomalies towards the correct direction. However, the result from time-lag CIGs inversion, as shown in Figure 13(a), is not satisfactory. The anomaly is not reconstructed successfully and we can observe the artifacts in the final result. Finally, we analyze the images migrated with the inverted models in all methods. The images in Figure 6(c) and Figure 10(c) are flatter than the image in Figure 3(c). This implies the models obtained with space-lag CIGs and CIPs inversion are better optimized than the model obtained with time-lag CIGs inversion. To summarize, the inversions with space-lag CIGs and CIPs converge faster than the inversion with time-lag CIGs. Also, the model are more accurately reconstructed in the inversions with space-lag CIGs and CIPs. Furthermore, the images migrated using the inverted models from space-lag CIGs and CIPs methods are more coherent than the image migrated with the inverted model from time-lag CIGs method.

## 4 DISCUSSION

We use the synthetic examples in the preceding section to illustrate the workflow of image-domain WI implemented with different image gathers. An important feature for image-domain WI is that the quality of the image is improved for all these formulations, as indicated by the more continuous and coherent image. The improvements can be further confirmed by observing better focusing property of reflections in the image gathers after the inversion. One common element for all these inversions is the penalty operator, which annihilates the energy at zero lags and highlights the energy outside zero lags due to the velocity model error.

The optimization procedure for both CIPs and space-lag CIGs recovers the anomalies in the subsurface, with the anomalies in the correct position and sign. In fact, we notice that there is plenty of similarity between the approaches of space-lag CIGs and CIPs. The kinematics of the residual

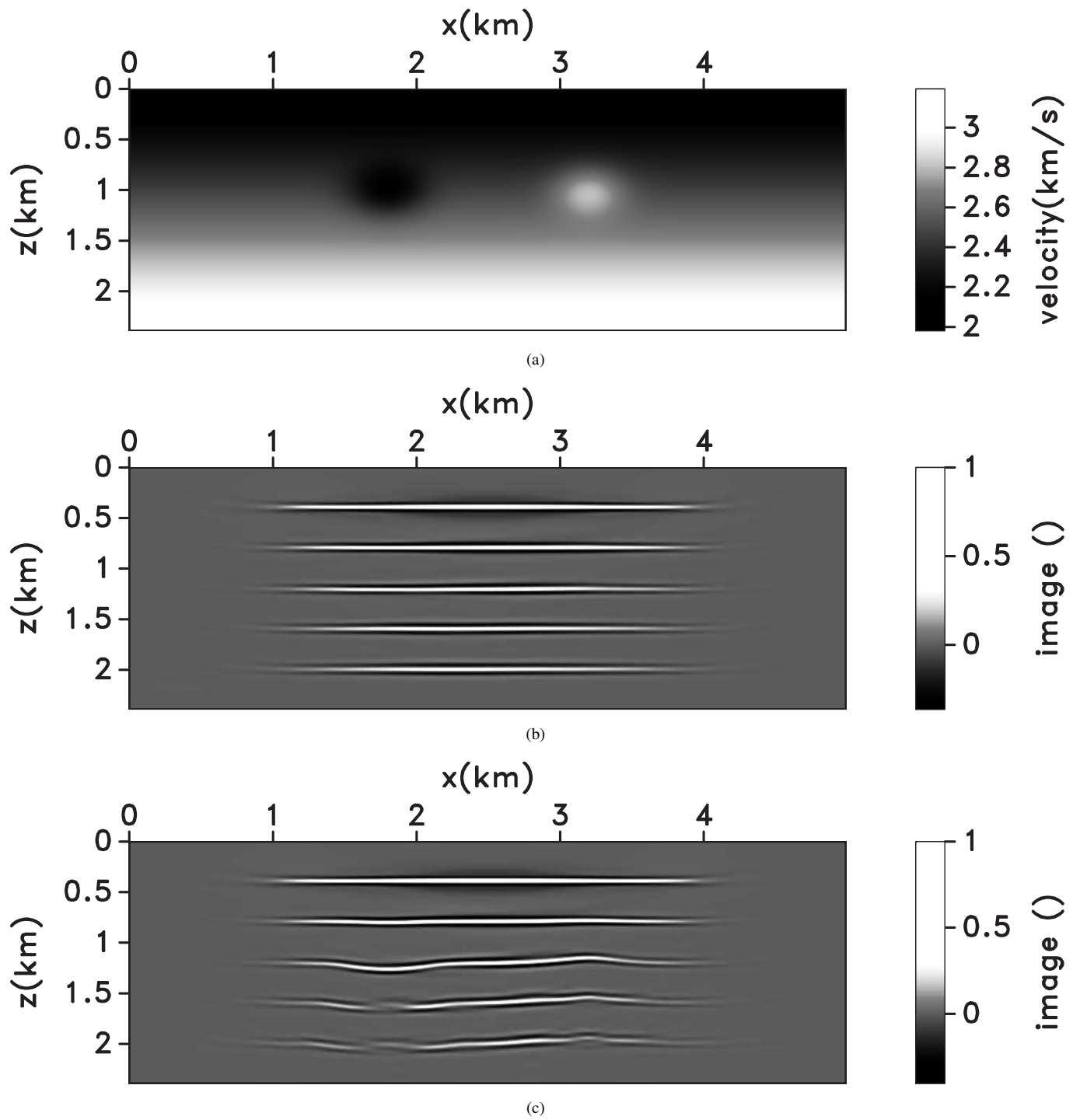
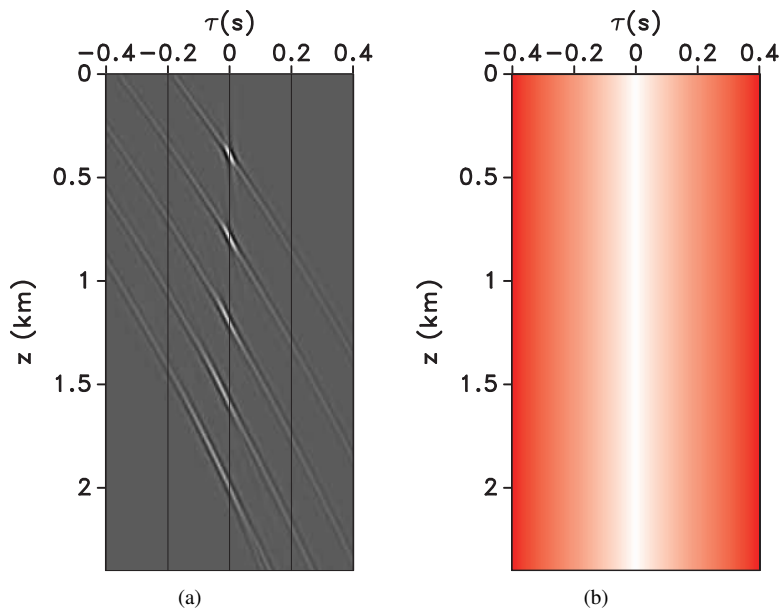


Figure 1. (a) The true velocity model. (b) The image migrated with the true velocity model. (c) The image migrated with the initial velocity model.



**Figure 2.** (a) An example of time-lag CIGs corresponding to the initial velocity model. (b) The penalty operator.

moveout due to the velocity model error are similar. Consequently, we should expect that the final results, e.g. the updated models and the corresponding migrated images, are similar. However, the OF corresponding to the inversion with CIPs shows some oscillations in later iterations. Such an oscillation is not observed in the inversion with space-lag CIGs. We speculate that such fluctuations are due to placing CIPs at different locations at each iteration. On the other hand, the inversion with time-lag CIGs is less successful. The reason is that reflections in time-lag CIGs not only focus at zero lag, but also spread energy at non-zero lags when the velocity model is correct. When the velocity is incorrect, the focus of energy shifts but such a change is difficult to measure for the penalty operator. As a result, the OF is not sensitive to the velocity error and the optimization process does not converge easily.

The image-domain methods discussed here are all automatic approaches, and no manual picking is required to identify the image incoherency due to the velocity model error. Given the observations for the synthetic examples, we conclude that space-lag CIGs inversion is most stable one and the velocity estimation is successful. However, its expensive computational cost may prevent the application in large 3D model. The inversion of CIPs can render a similar result to that obtained by space-lag CIGs inversion. This suggests that CIPs can be used as an alternative, or even replacement for space-lag CIGs since the construction of CIPs is less computationally demanding, especially in 3D velocity model building applications.

## 5 CONCLUSIONS

WI can be formulated both in the data-domain or in the image-domain, and image-domain formulation can be implemented with conventional CIGs and extended CIPs. The same wavefields are used in all cases (i.e. the same wave-equation, the same sources and boundary conditions, etc), therefore these implementations are not at all different from this point of view. The data-domain OF applies a time-lag penalty to the correlation of the simulated and observed wavefields before summation over experiments. This OF uses correlations only on the surface at the known locations of the receivers. In contrast, the image-domain OF applies a penalty to the different image extensions (space-lag, time-lag, or complete lags) of the source and receiver wavefields after summation over experiments, i.e. it exploits the semblance principle. This OF uses correlations at any locations in the image, including surface locations. In all cases, the computation of the gradient is implemented using the adjoint-state method and the workflow applies equally well to different approaches. The synthetic examples suggest that the time-lag CIGs formulation is less effective compared to space-lag CIGs because the OF is less sensitive to the velocity model error. However, when the time-lags are combined with space-lags, which leads to the formulation based on CIPs, the inversion behaves similarly to space-lag CIGs but at a lower computational cost as the time-lags replace the depth in the construction of the gathers and CIPs are sparsely sampled in the image.

## 6 ACKNOWLEDGMENTS

This work is supported by the sponsors of the Consortium Project on Seismic Inverse Methods for Complex

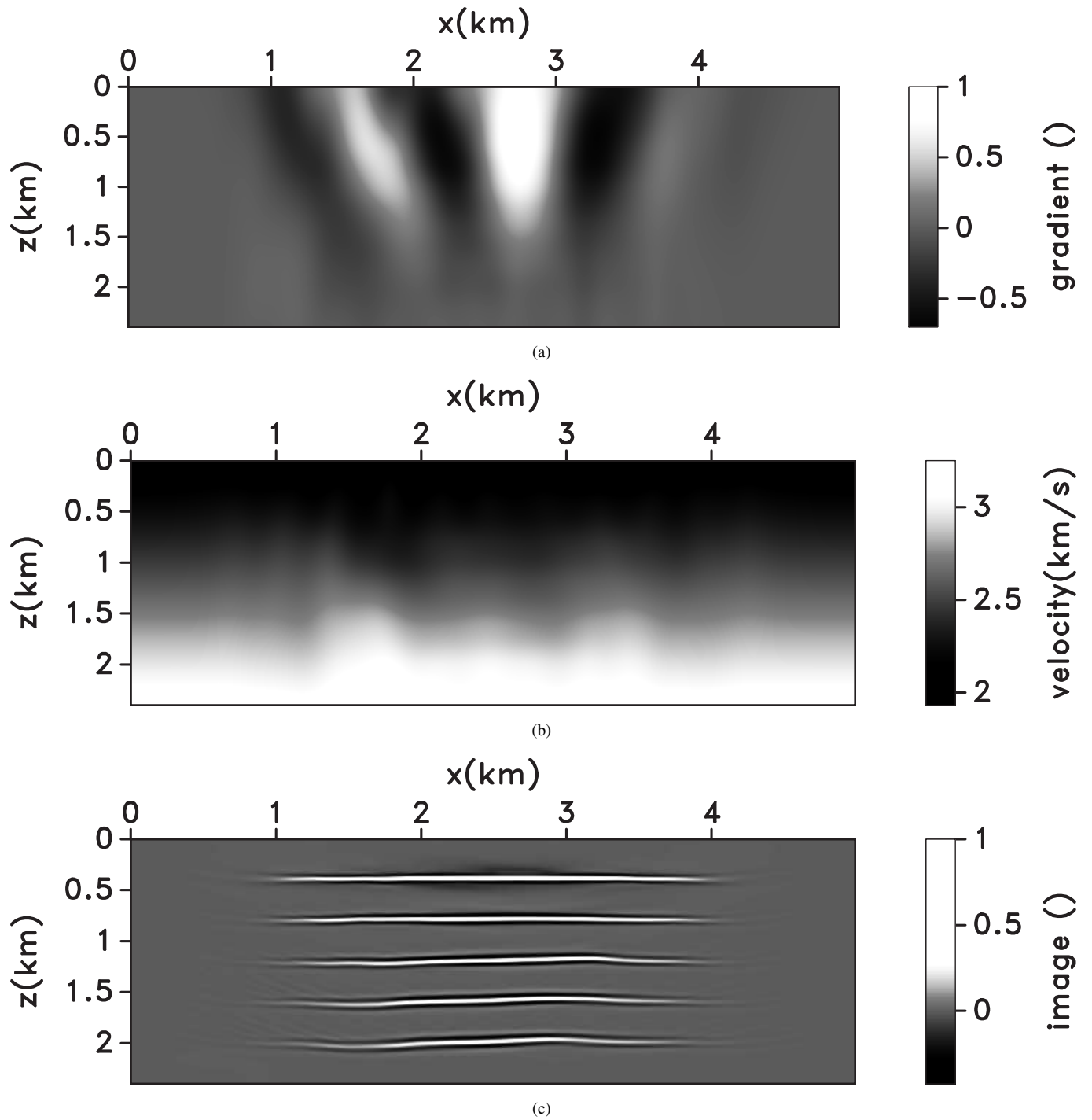


**Figure 3.** (a) The gradient computed at first iteration using equation 15. (b) The inverted velocity model. (c) The image migrated with the inverted velocity model.

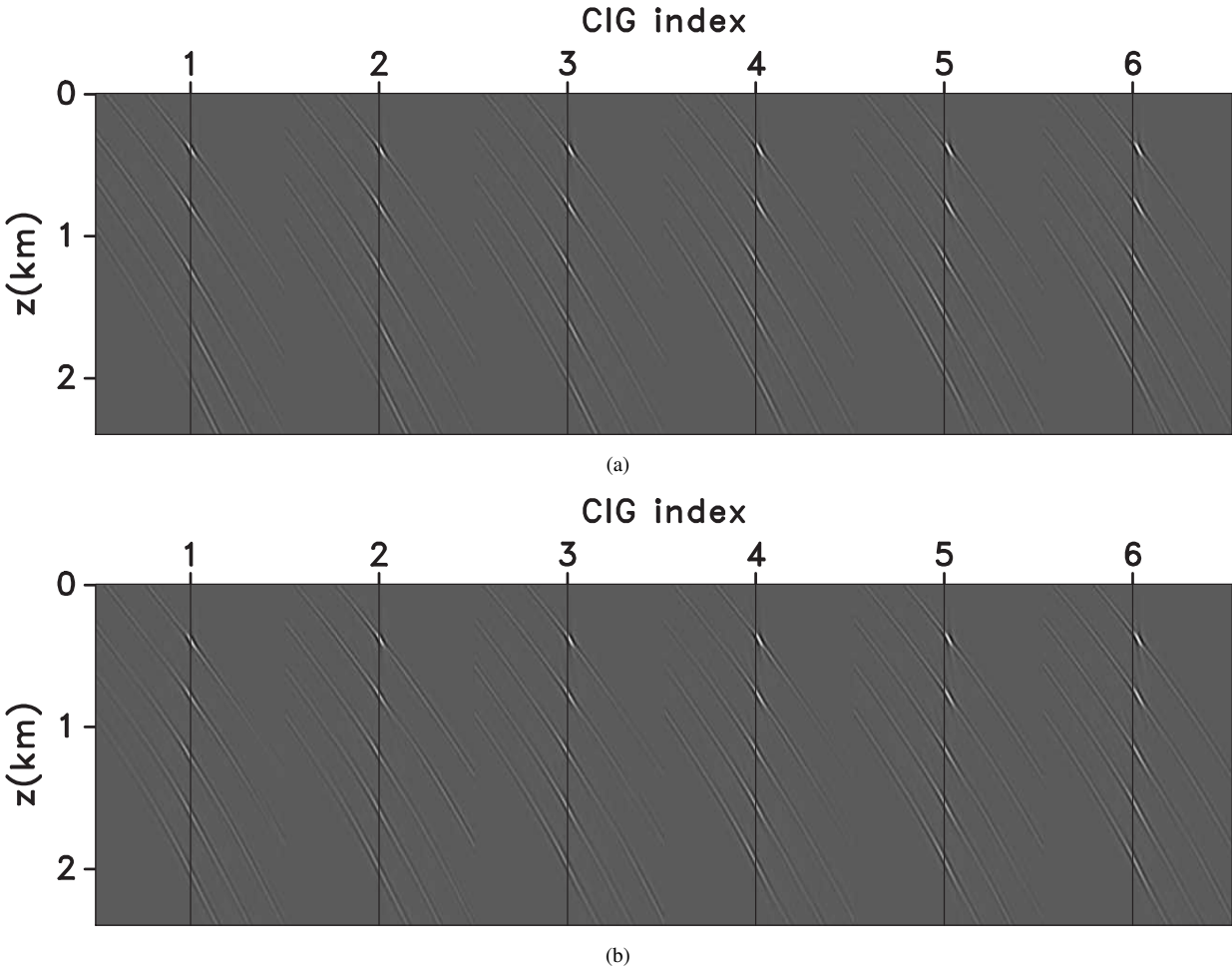


**Figure 4.** Time-lag CIGs migrated with (a) the initial velocity model, and (b) the inverted velocity model. The horizontal axis represents the CIG index. The gathers are selected every 0.2km, started at  $x = 1.9$  km.

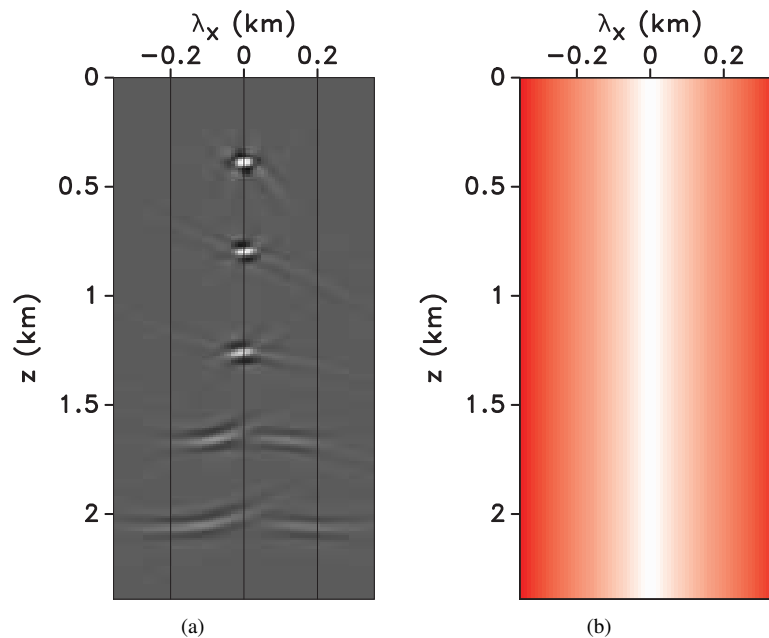


**Figure 5.** (a) An example of space-lag CIGs corresponding to the initial velocity model. (b) The penalty operator.

Structures at the Center for Wave Phenomena. The reproducible numeric examples in this paper use the Madagascar open-source software package freely available from <http://www.reproducibility.org>.

## REFERENCES

- Al-Yahya, K., 1989, Velocity analysis by iterative profile migration: *Geophysics*, **54**, 718–729.
- Biondi, B., and W. Symes, 2004, Angle-domain common-image gathers for migration velocity analysis by wavefield-continuation imaging: *Geophysics*, **69**, 1283–1298.
- Cullison, T., 2011, An image guided method for automatically picking common-image-point gather locations from seismic images: Master thesis, Colorado School of Mines.
- Etgen, J., S. H. Gray, and Y. Zhang, 2009, An overview of depth imaging in exploration geophysics: *Geophysics*, **74**, WCA5–WCA17.
- Gray, S. H., J. Etgen, J. Dellinger, and D. Whitmore, 2001, Seismic migration problems and solutions: *Geophysics*, **66**, 1622–1640.
- Nemeth, T., 1995, Velocity estimation using tomographic depth-focusing analysis: 65th Annual International Meeting, SEG, Expanded Abstracts, 465–468.
- Parker, R. L., 1994, *Geophysical inverse theory*: Princeton Univ. Press.
- Plessix, R.-E., 2006, A review of the adjoint state method for computing the gradient of a functional with geophysical applications: *Geophysical Journal International*, **167**, 495–503.
- , 2009, Three-dimensional frequency-domain full-waveform inversion with an iterative solver: *Geophysics*, **74**, WCC53–WCC61.
- Pratt, R. G., 1999, Seismic waveform inversion in the frequency domain, Part 1: Theory and verification in a physical scale model: *Geophysics*, **64**, 888–901.
- Rickett, J., and P. Sava, 2002, Offset and angle-domain common image-point gathers for shot-profile migration: *Geophysics*, **67**, 883–889.
- Sava, P., and B. Biondi, 2004a, Wave-equation migration velocity analysis - I: Theory: *Geophysical Prospecting*, **52**, 593–606.
- , 2004b, Wave-equation migration velocity analysis - II: Subsalt imaging examples: *Geophysical Prospecting*, **52**, 607–623.
- Sava, P., B. Biondi, and J. Etgen, 2005, Wave-equation migration velocity analysis by focusing diffractions and reflections: *Geophysics*, **70**, U19–U27.
- Sava, P., and S. Fomel, 2003, Angle-domain common image gathers by wavefield continuation methods: *Geophysics*, **68**, 1065–1074.
- , 2006, Time-shift imaging condition in seismic migration: *Geophysics*, **71**, S209–S217.
- Sava, P., and I. Vasconcelos, 2011, Extended imaging condition for wave-equation migration: *Geophysical Prospecting*, **59**, 35–55.
- Sava, P., and I. Vlad, 2008, Numeric implementation of wave-equation migration velocity analysis operators: *Geophysics*, **73**, VE145–VE159.
- , 2011, Wide-azimuth angle gathers for wave-equation migration: *Geophysics*, submitted for publication.
- Shen, P., and H. Calandra, 2005, One-way waveform inversion within the framework of adjoint state differential

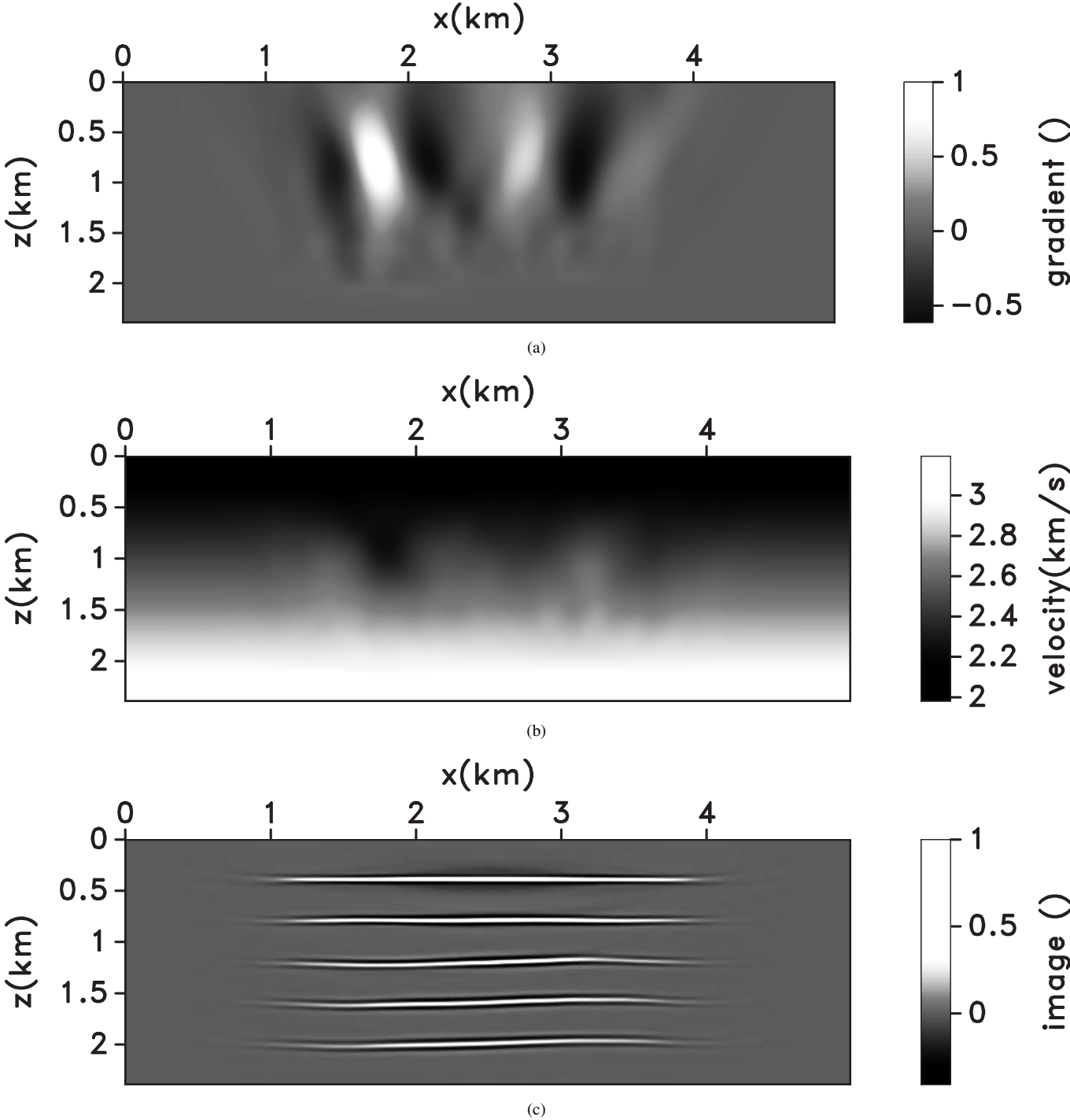
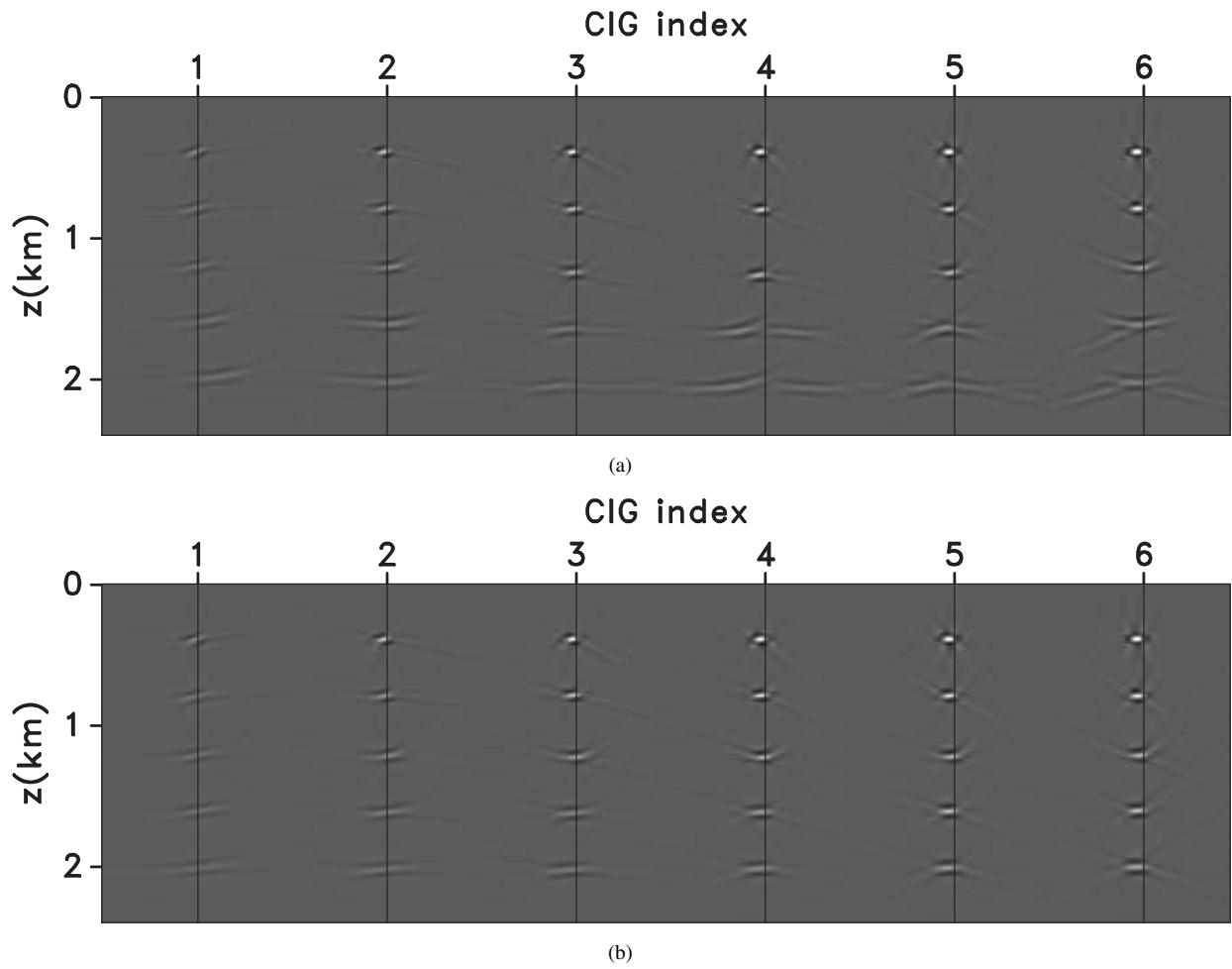
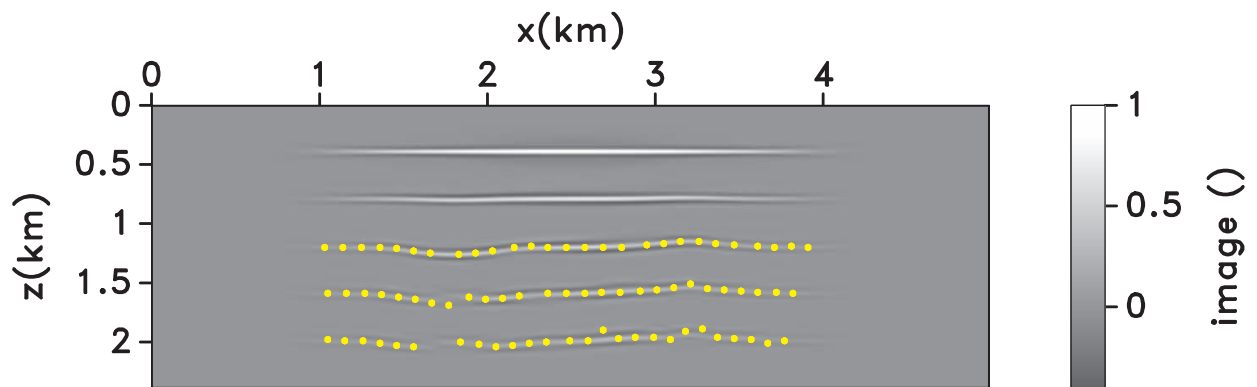


Figure 6. (a) The gradient computed at first iteration using equation 15. (b) The inverted velocity model. (c) The image migrated with the inverted velocity model.



**Figure 7.** Space-lag CIGs migrated with (a) the initial velocity model, and (b) the inverted velocity model. The horizontal axis represents the CIG index. The gathers are selected every 0.2km, started at  $x = 1.9$  km.



**Figure 8.** The locations of the constructed CIPs.

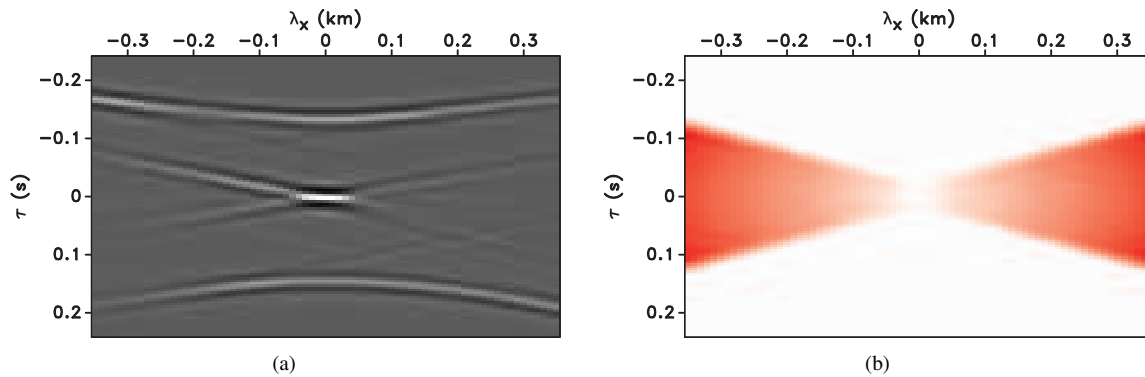


**Figure 9.** (a) An example of CIPs corresponding to the initial velocity model. (b) The penalty operator combined with the muting window to remove crosstalks.

migration: 75th Annual International Meeting, SEG, Expanded Abstracts, 1709–1712.

Shen, P., and W. W. Symes, 2008, Automatic velocity analysis via shot profile migration: *Geophysics*, **73**, VE49–VE59.

Sirgue, L., and R. Pratt, 2004, Efficient waveform inversion and imaging: A strategy for selecting temporal frequencies: *Geophysics*, **69**, 231–248.

Symes, W., 2009, Migration velocity analysis and waveform inversion: *Geophysical Prospecting*, **56**, 765–790.

Symes, W. W., 2008, Migration velocity analysis and waveform inversion: *Geophysical Prospecting*, **56**, 765–790.

Symes, W. W., and J. J. Carazzone, 1991, Velocity inversion by differential semblance optimization: *Geophysics*, **56**, 654–663.

Tarantola, A., 1984, Inversion of seismic reflection data in the acoustic approximation: *Geophysics*, **49**, 1259–1266.

van Leeuwen, T., and W. A. Mulder, 2010, A correlation-based misfit criterion for wave-equation traveltime tomography: *Geophysical Journal International*, **182**, 1383–1394.

Vasconcelos, I., P. Sava, and H. Douma, 2010, Nonlinear extended images via image-domain interferometry: *Geophysics*, **75**, SA105–SA115.

Vigh, D., and E. W. Starr, 2008, 3D prestack plane-wave, full-waveform inversion: *Geophysics*, **73**, VE135–VE144.

Virieux, J., and S. Operto, 2009, An overview of full-waveform inversion in exploration geophysics: *Geophysics*, **74**, WCC1–WCC26.

Wang, B., F. Qin, V. Dirks, P. Guillaume, F. Audebert, and D. Epili, 2005, 3d finite angle tomography based on focusing analysis: 78th Annual International Meeting, SEG, Expanded Abstracts, 2546–2549.

Woodward, M., D. Nichols, O. Zdraveva, P. Whitfield, and T. Johns, 2008, A decade of tomography: *Geophysics*, **73**, VE5–VE11.

Woodward, M. J., 1992, Wave-equation tomography: *Geophysics*, **57**, 15–26.

Yang, T., and P. Sava, 2010a, Moveout analysis of wave-equation extended images: *Geophysics*, **75**, 151–161.

———, 2010b, Wave-equation migration velocity analysis with extended common-image-point gathers: Presented at

the 80th Annual International Meeting, SEG, Expanded abstracts.

———, 2010c, Wave-equation migration velocity analysis with time-lag imaging: *Geophysical Prospecting*, submitted for publication.

Yilmaz, O., 2001, *Seismic Data Analysis* (2nd edition): Society of Exploration Geophysicists.

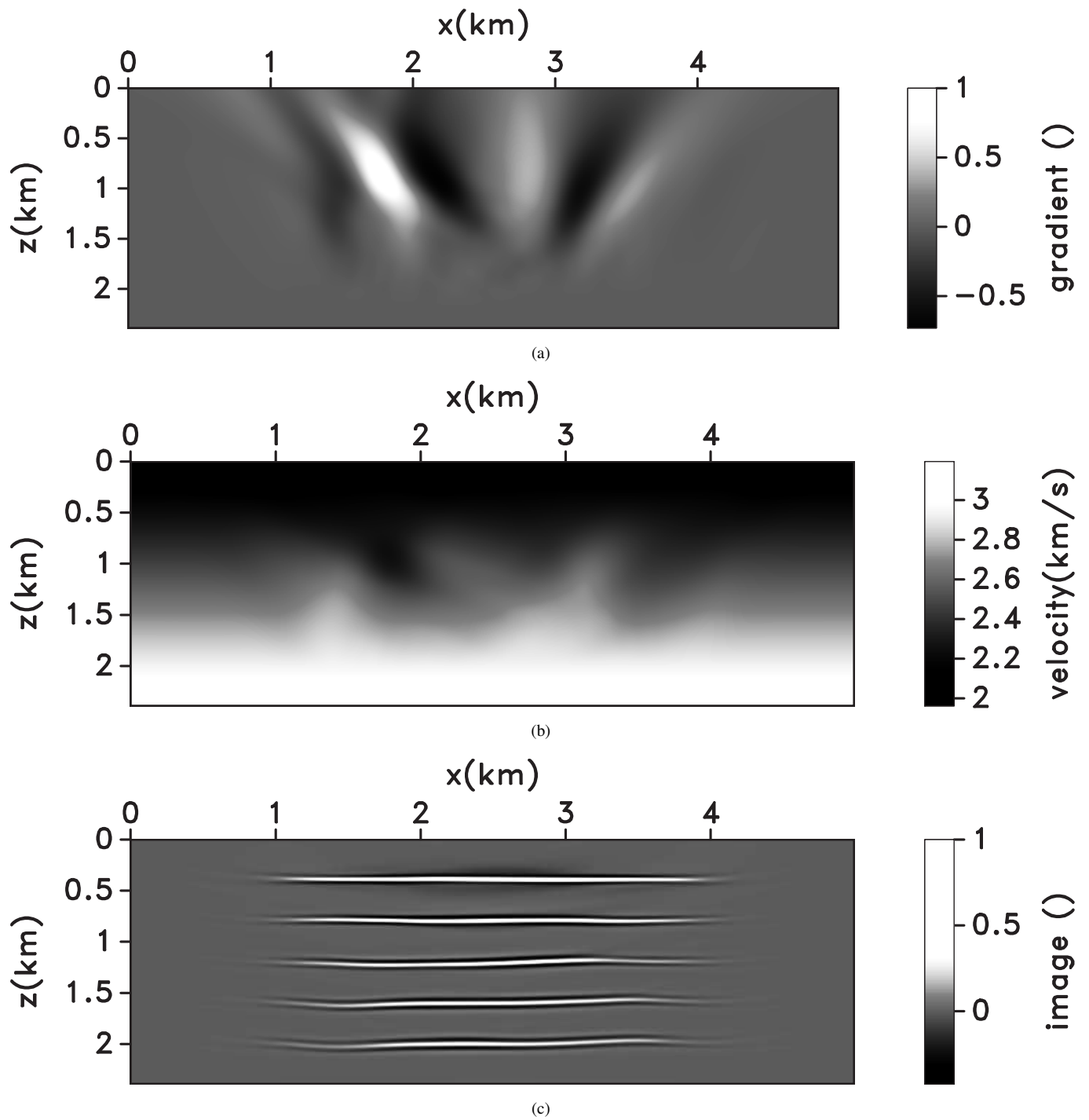


**Figure 10.** (a) The gradient computed at first iteration using equation 15. (b) The inverted velocity model. (c) The image migrated with the inverted velocity model.

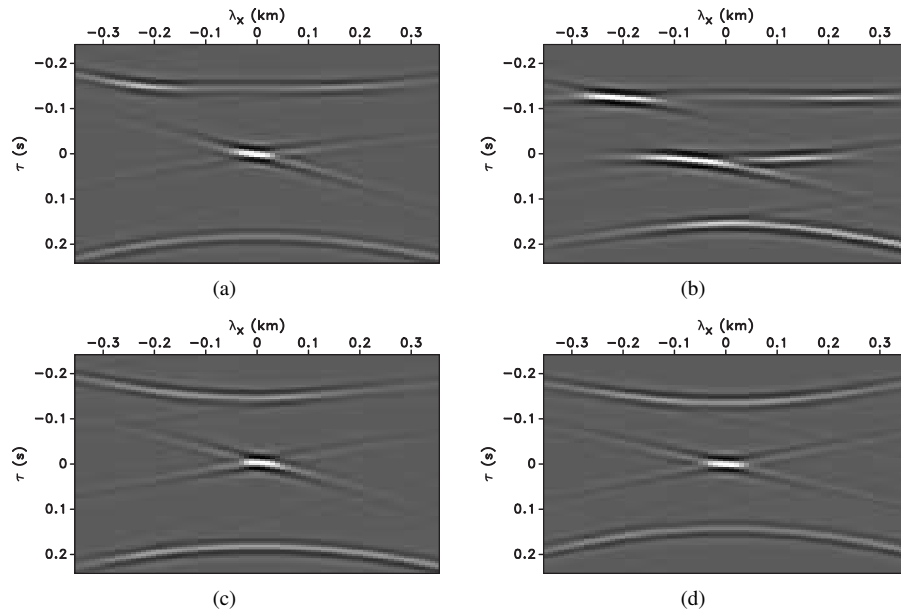


**Figure 11.** The comparison between CIPs before and after the inversion. CIPs before the inversion sampled at (a)  $x=1.85$  km,  $z=1.26$  km, (b)  $x=1.77$  km,  $z=1.69$  km. CIPs after the inversion sampled at (a)  $x=1.85$  km,  $z=1.22$  km, (b)  $x=1.77$  km,  $z=1.62$  km.

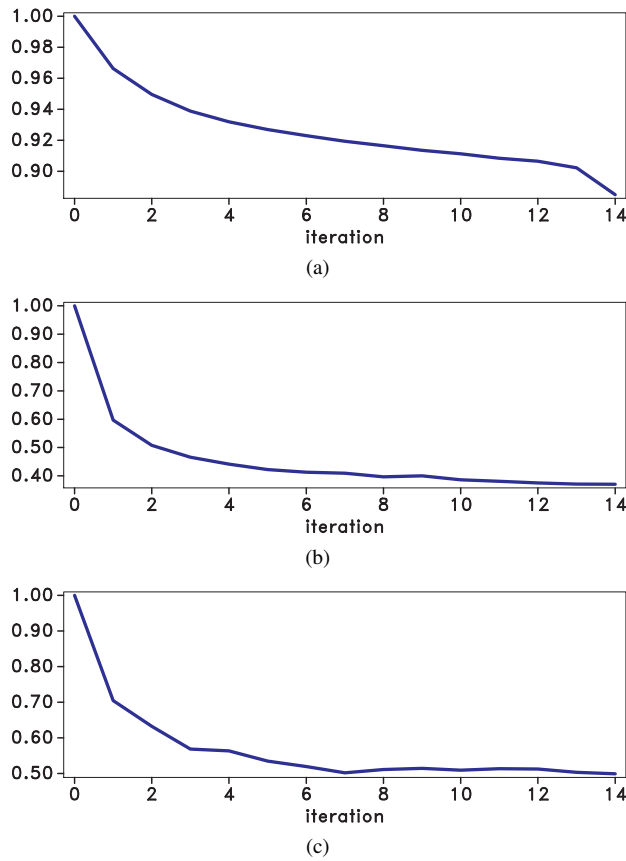


**Figure 12.** (a) The objective OF for the inversion with time-lag CIGs. (b) The OF curve for the inversion with space-lag CIGs. (c) The OF curve for the inversion with CIPs.

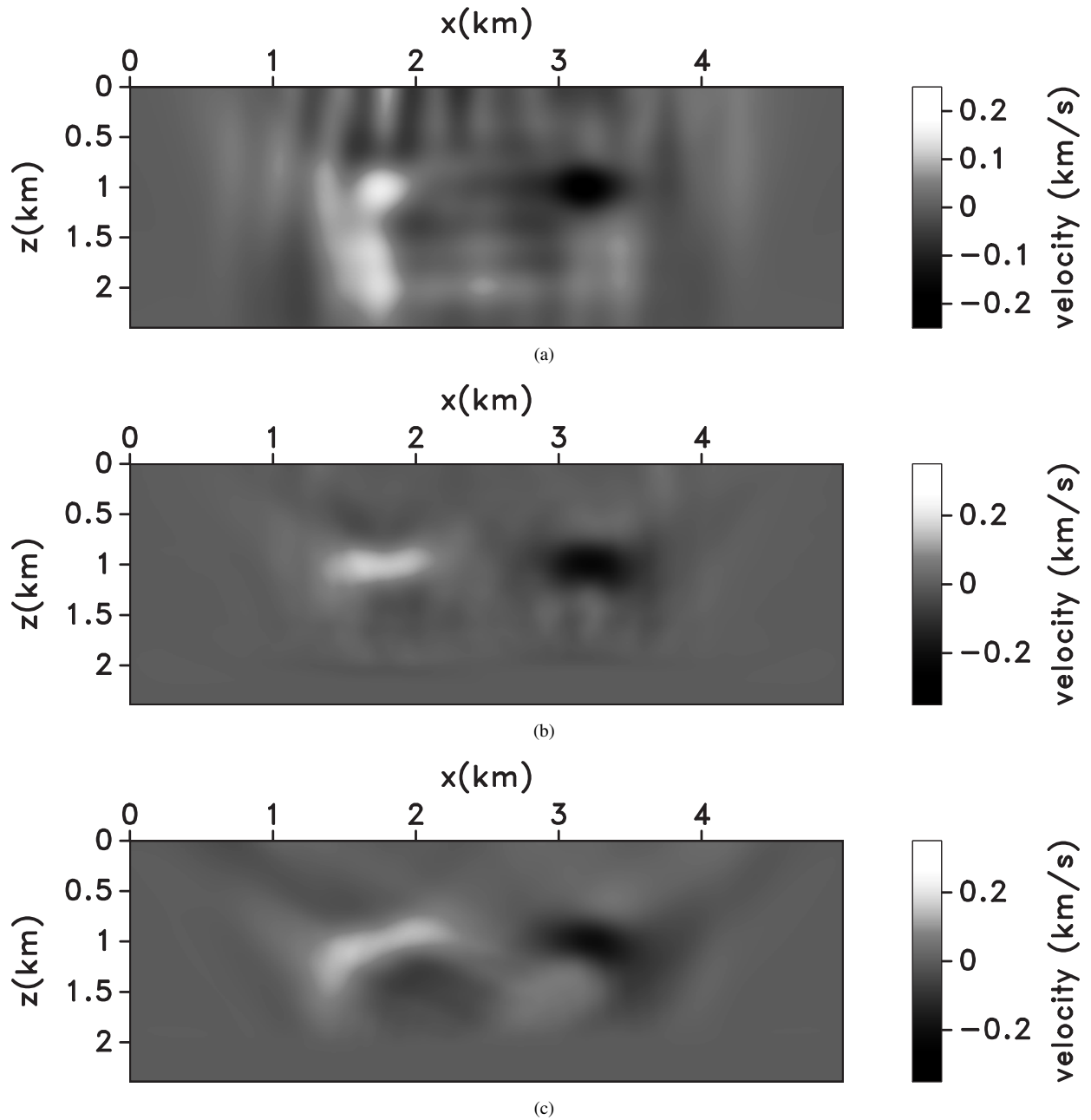


**Figure 13.** (a) The difference between true and inverted anomaly for the inversion with time-lag CIGs. (b) The difference between true and inverted anomaly for the inversion with space-lag CIGs. (c) The difference between true and inverted anomaly for the inversion with CIPs.

